

Journal of Biomedical Optics

SPIEDigitalLibrary.org/jbo

Evanescent field shapes excitation profile under axial epi-illumination

Thomas P. Burghardt

Evanescient field shapes excitation profile under axial epi-illumination

Thomas P. Burghardt

Mayo Clinic Rochester, Department of Biochemistry and Molecular Biology and Department of Physiology and Biomedical Engineering, Rochester, Minnesota

Abstract. Axial epi-illuminating light transmitting a >1.3 -numerical-aperture microscope objective creates an excitation volume at focus with size and shape dictated by diffraction and due to refraction by the objective and by the coverslip interface separating a specimen in aqueous buffer from the oil immersion objective. The evanescent field on the coverslip aqueous side affects primarily the excitation volume axial dimension as the specimen in focus approaches the interface to within a few hundred nanometers. Following excitation, an excited stationary dipole moment emits fluorescence in a spatially varying pattern collected over the large objective aperture. Collected light propagates in parallel rays toward the tube lens that forms a real three-dimensional image that is decoded to identify dipole orientation. An integral representation of the excitation and emitted fields for infinity-corrected optics—including effects of finite conjugate illumination, fluorescence emission near an interface, emitter dipole orientation, spherical aberration, light transmission through a dichroic filter, and for real microscopic specifications—accurately models observed field intensities including the substantial excitation from the evanescent field. The goal is to develop and verify the practical depiction of excitation and emission in a real microscope for quantitative interpretation of the 3-D emission pattern. © 2012 Society of Photo-Optical Instrumentation Engineers (SPIE). [DOI: [10.1117/1.JBO.17.6.066021](https://doi.org/10.1117/1.JBO.17.6.066021)]

Keywords: axial epi-illumination; evanescent excitation; microfluidic device; near-field emission; dipole orientation.

Paper 12054 received Jan. 26, 2012; revised manuscript received Apr. 16, 2012; accepted for publication May 8, 2012; published online Jun. 8, 2012.

1 Introduction

Single-molecule biophysics has changed our understanding of protein structure–function relationships, notably in molecular motors and ion channels.¹ The single-molecule approach for molecular motors often uses a visible fluorescence signal detectable in a microscope to report protein position,² orientation,³ or conformation.⁴ The information is used to deduce the probability distribution characteristic for the detected molecular parameter. The signal of interest is detected in the presence of background fluorescence due to other labeled proteins or unrelated intrinsic fluorescence, and maximal signal-to-noise ratio (SNR) is a high priority. Conditions are optimal when the detection volume, defined by the maximal fluorophore concentration at which a single fluorophore is the major contributor to the total fluorescence signal, is smallest. Even when fluorophores are selectively photoactivated for fluorescence, the minimal detection volume assists in sparse activation and selective detection of signal over background.

Axial epi-illumination introduces excitation in wide-field or confocal microscopy using light refraction by the objective to form the illuminated volume. Axial rays fill the objective back focal plane (BFP), then form a diffraction-limited 3-D spot at the focal plane. The highest numerical-aperture (NA) objective forms the smallest illuminated volume that, with plane-polarized incident light, has a different characteristic length in each dimension. Focal-plane dimension characteristics are similar, but the larger one lies in the direction of the electric

field vector. The axial dimension characteristic is longer than either lateral dimension. Calculation shows that the axial characteristic becomes equivalent to the lateral characteristic when evanescent field contributions to the total field are significant. I demonstrate the significant contribution of the evanescent field to excitation using a microfluidic water-filled chamber with top and bottom formed by glass coverslips separated by $\sim 20\ \mu\text{m}$. The lower coverslip in optical contact with the objective supports evanescent field excitation on the aqueous side, whereas the upper coverslip, separated from the lower one by the $20\text{-}\mu\text{m}$ water layer, does not. Comparing axial profiles for fluorescent spheres at each interface confirms the narrowing effect of the evanescent field on the axial excitation profile.

I manipulate the excitation intensity axial profile to test the ability to simulate its shape by introducing two coherent laser beams through the objective. They propagate in parallel but travel different axial path lengths with relative phase difference δ . Superpositioned beams produce a standing wave at focus that splits the total intensity profile into two main lobes, provided δ is an integer multiple of one-half the illuminating light wavelength. Each main lobe has a full width at $1/e$ times the maximum (FWeM) narrower than the single-beam profile. This faceted axial excitation profile provides a device to detect its observed anomalous narrowing. The latter is probably due to an unmodeled coupling of the exciting field to the fluorescent dielectric sphere adsorbed to the coverslip. The effect suggests that the nanosphere textured planar coverslip interface could be engineered to lower exciting beam profile width beyond diffraction-limited resolution.

Address all correspondence to: Thomas P. Burghardt, Mayo Clinic Rochester, Department of Biochemistry and Molecular Biology, Rochester, Minnesota 55905. Tel: 507 284 8120; Fax: 507 284 9349; E-mail: burghardt@mayo.edu.

The two-beam focused interference pattern converges to a minimum at the focal point at infinite conjugate, but the pattern is adaptable by finite conjugate illumination of the objective using a translating large-diameter, long-focal-length lens (LFL) in the exciting beam expander. Axial LFL translation axially shifts the bimodal excitation profile to have a maximum at focus while introducing spherical aberration. These observations demonstrate profile adaptability by use of the LFL. Finite conjugate illumination was used to compensate for aberrations introduced by specimen refractive index inhomogeneities⁵ and could likewise be used on biological samples to correct for sample inhomogeneities affecting excitation focus. The objective correction collar nominally corrects for temperature and coverslip thickness variability. Finite conjugate illumination can separately adapt excitation. In combination, excitation and emission pathways are made independent such that the objective correction collar is first adjusted to improve fluorescence image sharpness followed by adjustment of the LFL to maximize fluorescence intensity and possibly resolution. Separate excitation and emission pathway corrections may be most advantageous in imaging applications where exciting and emitting wavelengths are disparate, such as multiphoton microscopy.

Light emitted by the dipole moment in the aqueous medium near the coverslip/aqueous interface is substantially affected by the interface⁶ before collection by the objective. Collected near-field and far-field emission is refracted into parallel propagating rays in image space that conserve their electric field polarization relative to the meridional plane upon passage through the objective. The meridional plane contains the incident and refracted rays and the optical axis. Parallel light transmits a dichroic filter set, then is converged by the tube lens into an image on the CCD camera. The tube lens is a low-aperture lens that with refraction likewise conserves the electric field polarization relative to the meridional plane. The polarization-conserving refractions are decoded at the detector, recognizing that interpretation depends on NA.⁷ Polarized emission from the dipole converts to a spatial representation at the BFP^{8,9} that the tube lens images as the point spread function (PSF) at the camera. The PSF devolves into six basis patterns that, in linear combination, specify any single-molecule emission pattern. From the observed emission pattern, the basis pattern coefficients that depend algebraically on dipole orientation are deduced.¹⁰ The basis patterns also depend on the PSF axial dimension, as pointed out previously.¹⁰ I developed axial dependence in basis patterns in this work due to its significance for removing ambiguity related to single-myosin orientation in skeletal and cardiac papillary muscle fibers.^{3,10}

I develop here a thorough numerical analysis of excitation and emission in a high-NA microscope. Computation uses real microscopic and auxiliary lens specifications, and observables are verified experimentally for accuracy. The analysis undertaken is critical for quantitative interpretation of a three-dimensional emission pattern reporting single-molecule orientation but develops a general approach to accurately estimate the polarized excitation and emission intensity at critical points within the microscope. I find that under normal axial epi-illumination excitation, the 1.45-NA oil immersion objective creates an evanescent field that substantially remodels the excitation volume for samples near the coverslip. I identify an anomalous axial distribution of exciting light using features of the axial profile produced by interfering exciting laser beams and demonstrate a method to selectively adapt exciting-beam focus to compensate for sample inhomogeneity or to exploit

special exciting-beam features. I also demonstrate that the shape of the PSF axial dimension depends on emitter dipole orientation. The latter property of the PSF is significant and useful but sometimes overlooked.

2 Methods

2.1 Sample Preparations

Red-orange carboxylate-modified 40-nm-diameter fluorescent spheres having excitation/emission maxima at 565/580 nm were from Molecular Probes (Life Technologies, Grand Island, NY). The stock was diluted 10^4 -fold into distilled water, giving a concentration of 1.4×10^{11} spheres/mL. Experiments were conducted at room temperature.

Experiments were performed in microfluidic channels constructed using the toner transfer method just as described earlier.¹¹ Figure 1(a) shows the channel pattern drawn in Adobe Photoshop at 1200-dpi resolution with each square pixel $\sim 20 \mu\text{m}$ on a side. Horizontal stripes are $100 \mu\text{m}$ wide, and the full pattern fits on a 22- by 30-mm #1 glass coverslip (~ 0.15 mm thick). The pattern was printed onto Toner Transfer Paper (Pulsar, Crawford, FL) using a Samsung Laserjet printer (model ML-3471ND) at 1200-dpi printing resolution. The pattern was transferred to a brass substrate cut from shim stock (0.032 inch thick, Amazon) using heat and brass etching performed with a 20% solution (w/v) of ammonium persulfate (APS, Sigma). Regions protected by the toner are not etched. The pattern was etched to a depth of $20 \mu\text{m}$ using the total substrate weight to monitor progress, and the depth was verified experimentally as described below.

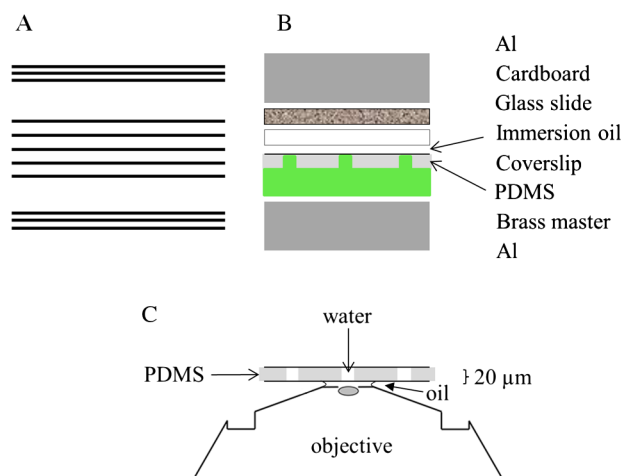


Fig. 1 Master pattern and assembly of the microfluidic chamber. (a) The master pattern drawn in Adobe Photoshop and printed onto toner transfer paper. Lines are $100 \mu\text{m}$ wide and 30 mm long. The pattern is transferred to a brass blank that is etched in APS. (b) Component assembly for making the PDMS spacer. Brass master has $20 \mu\text{m}$ deep channels filled with unpolymerized PDMS. After assembly, the multilayered system is clamped between 0.25-inch thick aluminum stock plates (Al) then heated to polymerize the PDMS. The spacer remains firmly attached to the coverslip but detaches from the brass master. (c) The completed microfluidic chamber formed from the coverslip, polymerized PDMS, and another coverslip placed on the top. Fluorescent spheres were dried down on the top coverslip before it was put on top of the chamber. Water was also added to fill the chamber before the top was put into place. Some spheres from the top coverslip detach and settle onto the bottom coverslip.

Polydimethylsiloxane (PDMS) was poured over the brass master, then a #1 glass coverslip was placed on top with care taken to avoid trapping air bubbles under the coverslip. A glass slide covered the coverslip but with immersion oil in between to prevent the coverslip sticking to the slide. Next a cardboard pad evenly distributed pressure from the 0.25-inch-thick aluminum stock plates (Al) as shown in Fig. 1(b). The assembly was clamped with a 1-inch binder clip, then heated to 80°C for 2 h to polymerize the PDMS as described previously.¹² After heating, the assembly was broken down and the coverslip recovered. On separating the coverslip from the brass master, the 20- μm -thick PDMS pattern tightly and smoothly adhered to the glass.

A watertight chamber was constructed from 3 coverslips. Two coverslips formed the top and bottom of the chamber, and the third was used to make 2- by 30-mm spacers separating the top and bottom coverslips. The spacers were arranged along the long edges of the coverslips. The spacers and coverslips formed a 0.15-mm-thick rectangular solid volume with opposite ends open. Fluorescent spheres were flowed into the open ends of the sample chamber and allowed to dry. A drop of distilled water was placed on the PDMS pattern—covered coverslip, then the bottom coverslip with dried fluorescent spheres attached was placed on top, sphere side down. The PDMS pattern and glass coverslip sandwich [see Fig. 1(c)] was placed on a slide holder with the PDMS-fixed coverslip on the bottom. The slide holder had a large hole cut out to allow access by the objective from the inverted microscope. After ~ 30 min, a sparse random distribution of fluorescent spheres was observed in the microscope, fixed to either the upper or lower glass surface. The surfaces were 20 μm apart, judging by the distance the objective traveled to move focus between the lower and upper surfaces. Spheres diffusing in solution were rarely observed with the objective focused on either glass surface. Most experiments were performed on fluorescent spheres fixed to the lower coverslip in optical contact with the objective. Some experiments were performed on fluorescent spheres fixed to the upper coverslip. The latter were separated from the lower coverslip by the 20- μm aqueous layer and were well beyond the evanescent field present at the lower coverslip. Fluorescent spheres were always in the aqueous medium.

2.2 Microscopy

Figure 2 shows the inverted microscope (Olympus IX71) with excitation and emission detection pathways. Double arrows indicate translating elements in the apparatus with their approximate spatial resolution. The 514.5-nm line from the argon ion laser (Innova 300, Coherent, Santa Clara, CA) is intensity modulated by the acousto-optic modulator (AOM) then linearly polarized by the Glan-Taylor (P) polarizer. The polarization rotator (PR) uses Fresnel Rhombs to rotate linearly polarized light to the desired orientation. Linearly polarized light, split into two beams at the interferometer (IF), travels different path lengths before rejoining. Path length difference is ~ 4 cm, well under the ~ 10 cm coherence length of the laser. The lower and upper path beams have relative path difference controlled to ~ 1 -nm precision using a nanopositioning piezo stage and controller (nano-bio 100, MCL, Madison, WI) that translates two mirrors in tandem within the box. The beam expander (BE) consists of a 4 \times or 10 \times microscope objective and a large-diameter, long-focal-length (250 mm) lens (LFL). The LFL translates with 25- μm resolution using a motorized

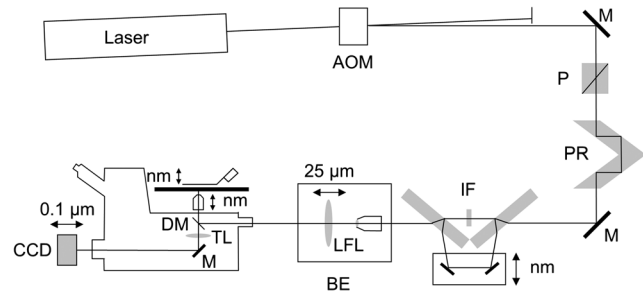


Fig. 2 Optical train for excitation and emission detection pathways serving the Olympus IX71 microscope. Double arrows indicate translating elements with the approximate spatial resolution indicated. Abbreviations: acousto-optic modulator (AOM), mirror (M), Glan-Taylor polarizer (P), polarization rotator (PR), interferometer (IF), beam expander (BE) containing the long focal length lens (LFL), dichroic mirror (DM), tube lens (TL), and CCD camera.

micrometer (Newport, Irvine CA). Exciting laser light enters the microscope, reflects at the dichroic mirror (DM), and is focused on the sample by the objective. The objective (Olympus planapo 60 \times , 1.45 NA, and 100 μm working distance) translates along the optical axis under manual control using the microscope focus and with nanometer precision using a piezo nanopositioner (C-Focus, MCL). Emitted light is collected by the objective, transmitted by the dichroic mirror, then focused by the tube lens (TL) onto the camera (CCD, Orca ER, Hamamatsu Photonics, Hamamatsu-City, Japan). A microscope stage with leadscrew drives and stepper motors translates the CCD camera with submicrometer resolution (LEP, Hawthorne, NY).

Overall computer control of the microscope is exercised through a custom-written Labview (National Instruments, Austin TX) routine and drivers supplied by the manufacturers. The Labview software coordinates image capture by the camera with movement of the various translating elements in or around the microscope. Translating elements are controlled via a RS232 port (LEP stage), a USB interface (MCL nanopositioners), or a D/A channel (NI6024 controlling the motorized micrometer driver). HCLImage (Hamamatsu) captures the images following triggering by the main Labview program via a counter output TTL pulse (NI6602).

An oil-immersion objective with a coverslip separating objective and aqueous sample and with NA larger than the refractive index of water (~ 1.3) will produce superpositioned evanescent and propagating fields on the aqueous side under epi-illumination when axial rays fill the BFP. Through-the-objective total internal reflection fluorescence (TIRF) confines the illuminating beam to regions in the BFP where only evanescent illumination will be produced at the sample.¹³

2.3 Interferometer

Figure 3 details the interferometer. Incident light propagates along the z -axis with incident and reflected beams confined to the xz -plane. Transparent gray slabs are glass optical flats of thickness L_1 . Light incident at angle σ transmits the air/glass interface then transmits (primary arm) or reflects (reflected arm) at the glass—air interface with the unbroken line depicting light paths. Broken lines indicate some of the uncaptured alternative light pathways. Neutral-density filter (NDF) slightly lowers intensity to balance primary and reflected beam intensities. Linear polarization is s-polarized at the flats in all experiments. Distance L_2 is the closest distance from mirror M and the optical

illumination could axially shift the intensity peaks offset from the focus such that one of them can be coincident with the objective focus at the origin. Shifted intensity peaks are useful for sample illumination but suffer from spherical aberration as described.⁵ There it is shown that finite conjugate illumination has aberration W , given by

$$W = \Delta w_{fc} \left\{ \cos[\theta] - 1 + \frac{\sin^2[\theta]}{2} \right\}, \quad (4)$$

for Δw_{fc} , the axial displacement of the beam image from the infinite conjugate focus due to displacement of the LFL. Next,

$$\Delta w_{fc} = \frac{f_1^2 \Delta L}{f_2^2 + \Delta L (f_1 + f_2 - p)}, \quad (5)$$

where $f_1 (= 3 \text{ mm})$ is the microscope objective focal length, p the distance separating the LFL and the microscope objective ($\sim 1 \text{ m}$), and ΔL the LFL displacement. LFL displacement dynamic range was 30 mm. Ray tracing through the beam expander indicated that this dynamic range corresponded to beam divergence or convergence of ≤ 0.1 deg.

2.7 Computation of Emission-Field Intensity and Detected Image

Divergent light collected by the objective converts to plane-polarized light rays propagating in parallel in image space toward the tube lens. Intensity patterns at the BFP represent the angular divergence of collected rays as a spatial intensity pattern separating the near-field from far-field emission of the fluorescent object.⁸ The BFP spatial intensity pattern from single-molecule fluorescence emission also uniquely quantifies emitter dipole orientation.⁹ The image space propagating light transmits the dichroic and barrier filters that impact the light polarization and the intensity pattern ultimately imaged by the tube lens on the CCD. The tube lens was air immersion with 180-mm focal length and radius of 12.5 mm in the IX71. The computation of the emitted field as it transmitted the objective, dichroic filter, tube lens, and then imaged on the camera was described previously.¹⁰

The emitted field at the CCD camera is the superposition of contributions from the emission dipole components. Like the lateral dependence, emitted field intensity axial dependence distinguishes emission from dipoles that are in the object plane (parallel) or normal to it (normal). Figure 4 indicates the emitted field intensity axial dependence from a normal (solid line) or parallel (dashed line) dipole. Normal dipole emission intensity approaches zero (compared to a parallel dipole) precisely at its image space focal point; however, the camera pixel integrates over a finite area in the image plane. Figure 4 shows an integrated intensity over the domain of a single CCD camera pixel. In this case, intensities are comparable between normal and parallel dipoles. Figure 4 also indicates that peak intensities differ for parallel and normal components. It is an aberration that is minimized but not eliminated by the objective compensating collar.

Alternatively, the axial emitted intensity is nominally approximated by a dipole orientation-independent profile¹⁶ given by

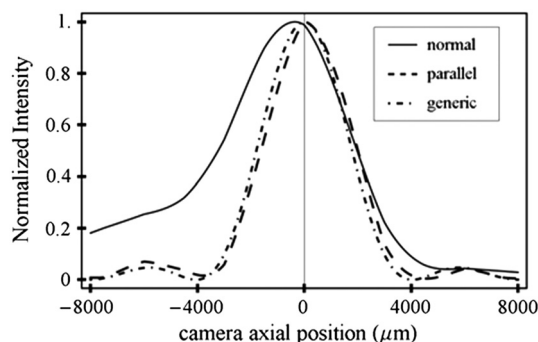


Fig. 4 Axial emission intensity profile at the CCD camera. Emitted fields from a single chromophore are the superposition of contributions from the emission dipole components. Emission dipoles in the object plane (parallel) or normal to it (normal) have different profiles given by the dashed or solid black lines. The generic profile (dot-dashed) is the standard model that does not distinguish between dipole components. Axial position of peak intensities differs for parallel and normal components.

$$I(z) = I(0) \left\{ \frac{\sin \left[\frac{z}{4} \frac{2\pi}{\lambda} \left(\frac{NA}{n_1} \right)^2 \right]}{\frac{z}{4} \frac{2\pi}{\lambda} \left(\frac{NA}{n_1} \right)^2} \right\}^2. \quad (6)$$

The axial profile from Eq. (6) is labeled “generic” in Fig. 4.

3 Results

3.1 Excitation Intensity Profile Versus Proximity to the Interface

Comparing axial epi-illumination excitation profiles for points inside the aqueous medium shows the evanescent field effect on intensity. Calculation shows that when $\beta = 0.8$ and for an exciting wavelength of 514.5 nm, an object on the coverslip interface sees an intensity profile with characteristic FWeM lengths of {380, 230, 368} nm for x -, y -, and z -dimensions. Linearly polarized incident electric field on the x -axis correlates with the widest profile. The y -dimension profile is significantly shorter than the others by close to a factor of 2. The axial dimension is intermediate but practically equal to the x -dimension profile. This contrasts with FWeM lengths of {382, 256, 518} nm seen by an object 20 μm from the coverslip interface in the aqueous medium but under otherwise identical conditions. In calculations, the evanescent field has a small effect on the lateral dimensions and a strong effect on the axial dimension. Axial FWeM length vs distance from the interface is plotted in Fig. 5. For objects on the interface, the axial half width at $1/e$ times maximum is 184 nm, which compares to the ~ 100 -nm depth of the evanescent field intensity in TIRF microscopy.¹⁷

I measured intensity profiles using the IX71 microscope, the 60 \times , 1.45-NA objective, and 40-nm-diameter fluorescent spheres immobilized on a glass surface, as described in Sec. 2. Experiments were conducted by focusing the objective on a fluorescent sphere specimen then translating the objective axially through a sawtooth pattern using the C-focus nanopositioner. Translation sweeps the exciting intensity profile through the point source that fluoresces proportionally to the exciting intensity. Figure 6 shows the objective translation sawtooth pattern (solid line) and the intensity observed for a one-beam

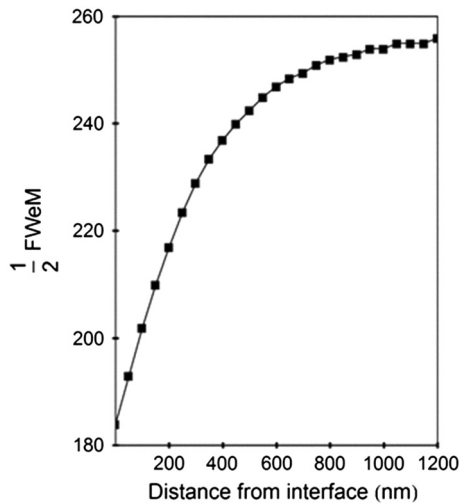


Fig. 5 Exciting light intensity axial half width at $1/e$ times maximum height versus distance from the interface for a point object detected with the 1.45-NA TIRF objective. The value at zero distance is for an object on the coverslip where the evanescent field is maximal.

(primary only) exciting light configuration (solid square). The righthand abscissa scale applies to the sawtooth curve with tickmarks indicating objective axial position. The lefthand abscissa scale applies to the intensity. In subsequent figures plotting the objective axial position (independent variable) versus fluorescence intensity (dependent variable), only the middle portion of the sawtooth pattern is shown where objective position changes monotonically. The translating objective emission profile used for simulating curves is the generic axial profile in Eq. (6) while neglecting aberration. The emission axial profile for the 1.45-NA objective is substantially broader than distinctive features in the excitation profiles and negligibly impacts fitting.

Both one- and two-beam configurations were used. Primary and reflected beams in the two-beam configurations had approximately equal intensities. The two-beam configurations, compared to their one-beam counterparts, provided more features to be aligned with simulation to enhance fitting reliability. Fitted curves (solid lines) for the two-beam configurations were generated as described in Sec. 2 with δ (relative phase shift between primary and reflected beams) and relative intensities of primary and reflected beams used as free parameters. In the one-beam configuration, there are no free fitting

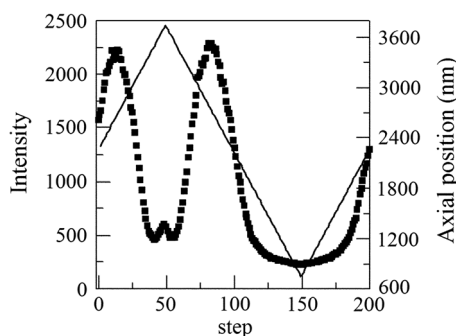


Fig. 6 Objective translation sawtooth pattern (solid line) and the intensity observed for a one-beam (primary only) exciting light configuration (solid square). The righthand abscissa scale applies to the sawtooth curve indicating objective position. The lefthand abscissa scale applies to the collected intensity in arbitrary units.

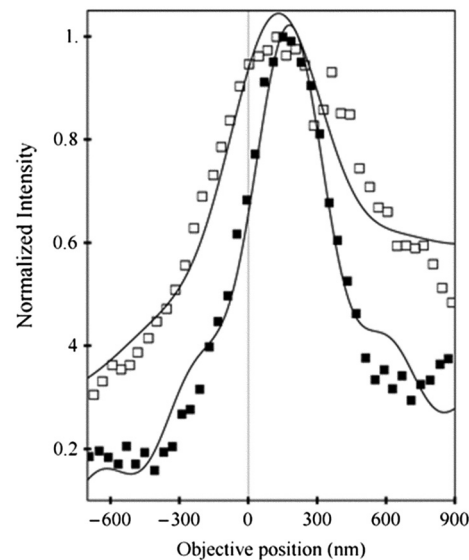


Fig. 7 Measured and simulated (solid line) exciting intensity profiles for the one-beam configuration and comparing profiles from fluorescent objects fixed to the lower (solid square) or upper (open square) glass coverslip. The narrower profile is in the presence of the evanescent field.

parameters. However, for either configuration, β is allowed to vary within $\sim 20\%$ of its nominal value of 0.8 or 2 for the 10 \times or 4 \times objective in the beam expander.

Figure 7 shows measured and simulated intensity profiles for the one-beam configuration and compares profiles from objects fixed to the lower or upper glass coverslip (see Fig. 1). Point fluorescent objects on the lower coverslip, where both evanescent and far fields contribute to excitation, produce the narrower profile (solid square). Point fluorescent objects on the upper coverslip produce the broader profile (open square). They are 20 μm from the lower coverslip across an intervening water layer and are subjected only to the far field. Computed profiles (solid lines) use $\beta = 2$ and differ only because of the evanescent field at the lower coverslip. Relative intensity between fluorescent point sources fixed to the lower and upper coverslips, not documented by the normalized intensity curves, is 2- to 4-fold higher at the lower coverslip where the evanescent field is present. Unpredicted oscillation of intensity near the extreme upstream objective translation may be due to aberration.

Figure 8 shows measured and simulated intensity profiles in several exciting light configurations all at the lower coverslip. Figure 8(a) shows intensity profiles for $\beta = 2$ and one-beam (primary only, open square) or two-beam (primary and reflected interfering, solid square) configurations. The computed one-beam profile has 1291 nm FWeM. According to simulation, the curve from the two-beam configuration corresponds to $\delta = 7\lambda/2$. The profile peaks broaden and separate with increasing δ . Relative beam intensity in the simulation for the two-beam configuration was 0.45 (primary) and 0.55 (reflected).

Figure 8(b) shows the intensity profile for $\beta = 2$ and two-beam configuration with $\delta = \lambda/2$. The profile has narrow peaks and ~ 450 -nm peak separation in agreement with simulation. A primary-only configuration has a 1006-nm FWeM axial profile in simulation (not shown). The dominant features of the observed profile are reproduced in simulation. Relative beam intensity in the simulation for the two-beam configuration was 0.47 and 0.53.

Figure 8(c) shows the intensity profile for $\beta = 0.8$ and two-beam configuration with $\delta = \lambda/2$. This is the narrowest observed profile, with ~ 250 nm peak separation. Simulation is unable to match the key profile features, including the main peak resonance positions and widths and, in particular, the side resonance that appears at ~ 500 nm. A primary-only configuration has a 368-nm FWeM axial profile in simulation (not shown). Relative beam intensity in the simulation for the two-beam configuration was 0.5 and 0.5.

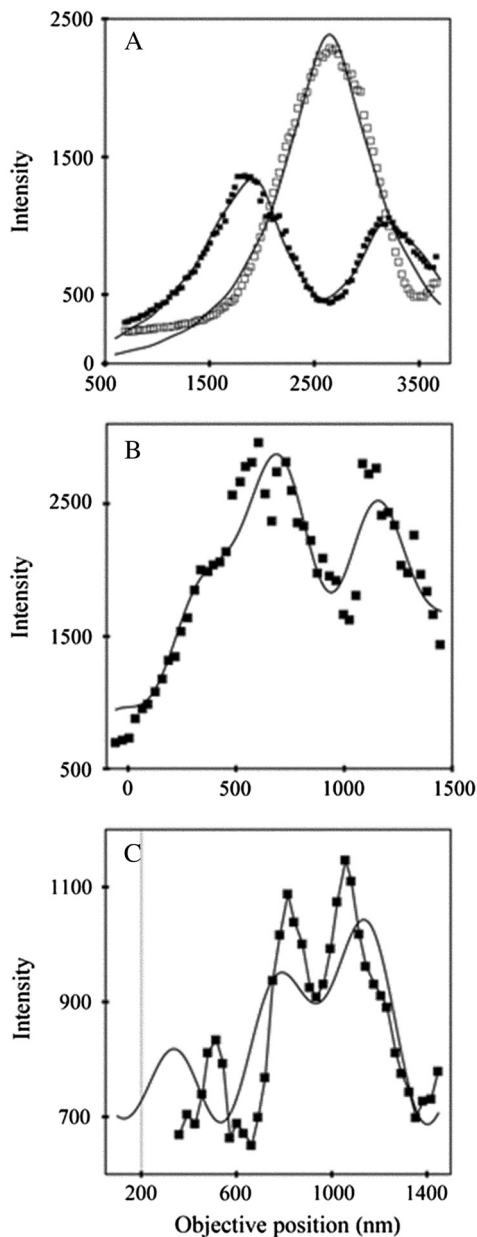


Fig. 8 Measured and simulated exciting intensity profiles in several exciting light configurations all for a fluorescent object at the lower coverslip. (a), Intensity profiles for $\beta = 2$ and one-beam (open square) or two-beam (solid square) configurations. The two-beam configuration corresponds to relative phase shift $\delta = 7\lambda/2$. (b), The intensity profile for $\beta = 2$ and two-beam configuration with $\delta = \lambda/2$. (c), The intensity profile for $\beta = 0.8$ and two-beam configuration with $\delta = \lambda/2$. This is the narrowest observed profile, with ~ 250 nm peak separation. Simulation does not accommodate key profile features including the main peak resonance positions and widths and the side resonance beyond the main peaks at 500 nm.

Simulation width in the axial dimension is strongly influenced by the evanescent field at the interface such that the profile narrows as the evanescent field contribution increases (Fig. 5). Results in Fig. 8(c) suggest that simulation underestimates the evanescent field effect, possibly because the planar model for the coverslip/aqueous interface is inadequate for the narrowest profile where the evanescent field effect is expected to be largest. Axial epi-illumination at the BFP falls within and without the critical angle ring dividing far- and evanescent-field exciting light, respectively, after refraction in the objective. The $\beta = 0.8$ BFP illumination has more of the total illumination falling beyond the critical angle ring, hence producing more evanescent exciting light. The 40-nm-diameter fluorescent sphere on the interface could enhance or focus evanescent field intensity in its vicinity that is more readily detected in the $\beta = 0.8$ profile.

3.2 Adapting the Exciting Intensity Profile

Figure 9 shows the measured exciting light intensity profile swept through the objective focus by using finite conjugate illumination and the fitted profile computed using Eqs. (4) and (5) and $\beta = 2$. Experiments were conducted by focusing the objective on a fluorescent sphere specimen at the lower coverslip using the primary-only exciting beam configuration then returning to the two-beam configuration and sweeping the LFL through a sawtooth pattern like that in Fig. 6. Shown is the emission intensity from the fluorescent sphere in the central section of the sawtooth where the LFL moves away from the microscope monotonically. The exciting light intensity profile is strictly proportional to fluorescence detected, confirming the bimodal axial intensity distribution for the two-beam configuration. The objective is not translating axially, hence no emission profile or emission aberration is involved; however, there is aberration in the exciting profile as discussed previously⁵ that I fully account for in simulation. The LFL translates the exciting light axial profile such that the peak intensity and emission focal plane are brought into coincidence. Figure 9 demonstrates the good agreement between computed and observed intensity profiles, indicating accurate modeling of the optical system.

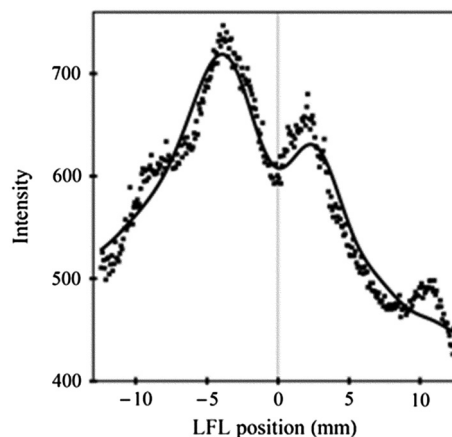


Fig. 9 Measured (solid square) and simulated (solid line) exciting light intensity profile vs position of long focal length lens (LFL) in the beam expander (Fig. 2). The LFL adapts the two-beam configuration excitation such that the exciting light peak intensity and emission focal plane are brought into coincidence at the fluorescence peaks. The LFL translates monotonically away from the microscope in its 25-mm travel.

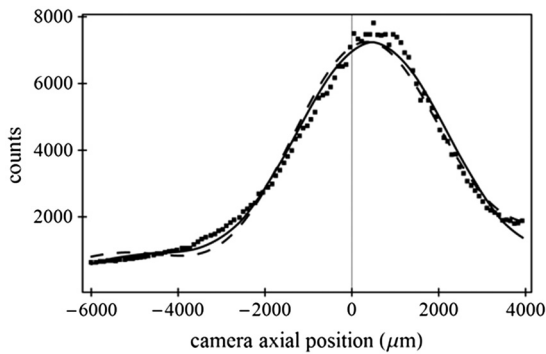


Fig. 10 Measured (solid square) and simulated (solid or dashed lines) axial dependence of the image field at the lateral focal point pixel from a 40-nm-diameter sphere fixed on the lower coverslip/aqueous interface. Light impinging on the center pixel of the sphere image is plotted as the CCD camera is scanned axially over ~ 10 mm. Best-fitting curves were generated for the integral representation (solid line) of the image field and from Eq. (6) (dashed line). The integral representation best accounts for observation.

The profiles also show that the excitation and emission focal planes can be adjusted independently using the LFL and the objective correction collar in concert.

3.3 Image Space Emission Profile

Figure 10 shows the detected axial dependence of the image field at the lateral focal point pixel from a 40-nm-diameter sphere fixed on the lower coverslip/aqueous interface (solid square). Experiments were conducted by CCD camera translation as described in Sec. 2, where light impinging on the center pixel of the sphere image is followed as the camera is scanned axially over ~ 10 mm using the LEP stage. Solid line curves are best fits estimated using Eq. (6) (dashed line) or by the integral representation (solid line) of the image field. The latter best accounts for observation and provides best-fit parameters for a linear combination of the emitting dipole components normal (78%) or parallel (22%) to the coverslip/aqueous interface.

The exciting evanescent field supports a large normal polarization component that varies from near zero to 70% of total intensity within $\sim 1/e$ of the peak intensity. A small sphere at the lower coverslip can experience almost twice the normally polarized light (depending on exact lateral position) as the same sphere at the upper coverslip owing to the dominance of the evanescent field. For a random distribution of probes, which I assume is the case for a fluorescent sphere conjugated to many chromophores, the observed fluorescence intensity follows the breakdown of exciting light polarization intensity. My image space emission profile analysis, summarized in Fig. 10, supports the higher normal component present in the total exciting field due to the evanescent field at the lower coverslip.

4 Discussion

Most biological imaging is done with scanning confocal microscopy, where a diffraction limited spot via axial epi-illumination is scanned over the sample while emitted light is collected through a confocal aperture. Smaller detection volumes providing higher-resolution images are achieved with higher-NA, oil-immersion objectives and glass coverslips. The highest

NA objectives available are TIRF objectives for through-the-objective total internal reflection because they achieve excitation incidence angles beyond critical angle for the glass/aqueous interface. Light incident beyond critical angle is non-propagating or evanescent on the aqueous side of the interface where its intensity decays exponentially with distance normal to the interface. The evanescent field depth is ~ 100 nm for green light and a 1.45-NA objective. Generally, TIRF or epi-illumination excitations pertain to evanescent or propagating field microscopies that are appropriate for different applications. I show here that the TIRF objective under common axial epi-illumination conditions produces an evanescent field that favorably remodels the excitation volume for samples near the coverslip.

Point source fluorescent spheres were imaged from a region where the excitation evanescent field contributes to excitation and from a region where the evanescent field is necessarily absent. To do so, I constructed a microfluidic PDMS spacer that separates two glass coverslips (Fig. 1). The lower coverslip optically contacts the oil immersion objective whereas the upper coverslip has an intervening 20- μm -thick slab of water. The 100- μm objective working distance ensures that either object can be brought into focus by vertical movement of the objective. Objects at the lower coverslip are subjected to both evanescent and propagating exciting fields whereas objects at the upper coverslip feel only the propagating field. Figure 7 shows a one-beam intensity profile measured by axial translation of the objective over ~ 1500 nm, indicating the narrowing effect of the evanescent field. Profile computation agrees with observation. Figure 5 indicates the expected half-width remodeling of the axial dependence for exciting light as a function of probe position relative to the lower coverslip interface. I also observed a 2- to 4-fold intensity enhancement for the fluorescent sphere at the lower coverslip that is attributable to the discontinuous enhancement of the exciting normal electric field on the aqueous side at the lower coverslip, the selective collection of near-field emission from a sphere at the lower coverslip, and the effect of light scattering in the intervening water layer on both exciting and emission light for the sphere at the upper coverslip. Other effects may be significant, including the presence of the aqueous/glass interface at the upper coverslip.

Point source fluorescent spheres were imaged at the lower coverslip by exciting light exiting an interferometer. Axial profiles varied depending on the ratio of objective aperture radius to beam waist radius, β , and on the relative path length difference, δ , between interfering primary and reflected beams. Figure 8 shows that the computed axial distribution closely resembles observation except for the narrowest profile that I was unable to reproduce in calculation. I propose that the planar model for the coverslip/aqueous interface is inadequate for the narrowest profile observed due to the specific enhancement of the evanescent field in the vicinity of the 40-nm-diameter dielectric fluorescent sphere on the interface. This effect could be exploited to engineer a nanosphere textured planar coverslip interface to diminish exciting beam axial profile width.

I also succeeded in adapting the exciting field focus using finite conjugate illumination in a manner that can be modeled using the parameters describing the lenses in the beam expander (see Fig. 2). Figure 9 indicates the effect of LFL translation on the intensity and shows that computed intensity closely resembles observation. Finite conjugate illumination separates excitation and emission focal planes, a property potentially useful for

color correction or multiphoton microscopy applications where exciting and emitting wavelengths differ widely.

Axial emission profile dependence on emitter dipole moment orientation is exemplified by the curves in Fig. 4 for dipole moments parallel or normal to the focal plane. I find that the emission profile depends significantly on dipole orientation. Curve fitting of the axial emission profile (Fig. 10) showed that for the fluorescent sphere at the lower coverslip, exciting light axial polarization from the evanescent field contributes substantially to the observed fluorescence. This is additional evidence for the significance of the evanescent field under axial epi-illumination excitation. It shows that evanescent excitation contributes to observed fluorescence whenever a TIRF objective is used and suggests that the sample material nearest the coverslip disproportionately contributes to the observed fluorescence signal.

The analysis undertaken is critical for quantitative interpretation of a 3-D emission pattern reporting single-molecule orientation but develops a general approach to accurately estimate the polarized excitation and emission intensity at critical points within the microscope. The experimental and numerical analysis of excitation and emission collection in an infinity-corrected TIRF microscope objective indicates wide agreement between observation and calculation with several unexpected findings and one exception. On the excitation side, computation shows that normal axial epi-illumination produces an evanescent field that significantly contributes to excitation of sample near the coverslip interface. Its excitation axial profile is equivalent in size to its excitation lateral profile and close to the evanescent field penetration depth under total internal reflection illumination. I verified this effect experimentally under practical experimental conditions using a novel microfluidic cell. An exception was noted for the narrowest excitation profiles produced in the two-beam configuration, when the exciting profile was observed to be narrower than the narrowest possible simulated profile for the conditions. I hypothesize that the 40-nm-diameter dielectric fluorescent sphere on the interface enhances evanescent field intensity in its vicinity that is detected by the narrowed profile. The effect suggests that a nanosphere textured planar coverslip interface could be engineered to lower exciting beam profile width beyond diffraction limited resolution. I demonstrated a method to selectively adapt exciting beam focus to compensate for sample inhomogeneity, to exploit special exciting beam features, or to correct wavelength dependent refraction by the objective. On the emission side, computation shows that dipole orientation has a significant dependence on the axial emission profile, unlike a generic profile that is independent of dipole orientation. I made use of this property to estimate the evanescent field contribution to excitation intensity under axial

epi-illumination and found approximate agreement with the expected presence of a substantial evanescent field.

Acknowledgments

This work was supported by NIH grants R01AR049277 and R01HL095572 and by the Mayo Foundation. The author gratefully acknowledges inspiration from Dude Burghardt.

References

1. T. P. Burghardt and K. Ajtai, "Single-molecule fluorescence characterization in native environment," *Biophys. Rev.* **2**(4), 159–167 (2010).
2. A. Yildiz et al., "Myosin V walks hand-over-hand: single fluorophore imaging with 1.5-nm localization," *Science* **300**(5628), 2061–2065 (2003).
3. T. P. Burghardt, M. P. Josephson, and K. Ajtai, "Single myosin cross-bridge orientation in cardiac papillary muscle detects lever-arm shear strain in transduction," *Biochemistry* **50**(36), 7809–7821 (2011).
4. Y. Gambin et al., "Visualizing a one-way protein encounter complex by ultrafast single-molecule mixing," *Nat. Methods* **8**(3), 239–241 (2011).
5. S. Stallinga, "Finite conjugate spherical aberration compensation in high numerical-aperture optical disc readout," *Appl. Opt.* **44**(34), 7307–7312 (2005).
6. E. H. Hellen and D. Axelrod, "Fluorescence emission at dielectric and metal-film interfaces," *J. Opt. Soc. Am. B* **4**(3), 337–350 (1987).
7. D. Axelrod, "Carbocyanine dye orientation in red cell membrane studied by microscopic fluorescence polarization," *Biophys. J.* **26**(3), 557–573 (1979).
8. A. Mattheyses and D. Axelrod, "Fluorescence emission patterns near glass and metal-coated surfaces investigated with back focal plane imaging," *J. Biomed. Opt.* **10**(5), 054007 (2005).
9. T. P. Burghardt and K. Ajtai, "Mapping microscope object polarized emission to the back focal plane pattern," *J. Biomed. Opt.* **14**(3), 034036 (2009).
10. T. P. Burghardt, "Single molecule fluorescence image patterns linked to dipole orientation and axial position: application to myosin cross-bridges in muscle fibers," *PLoS One* **6**(2), e16772 (2011).
11. C. J. Easley et al., "Rapid and inexpensive fabrication of polymeric microfluidic devices via toner transfer masking," *Lab Chip* **9**(8), 1119–1127 (2009).
12. B. H. Jo et al., "Three-dimensional micro-channel fabrication in polydimethylsiloxane (PDMS) elastomer," *J. Microelectromech. Syst.* **9**(1), 76–81 (2000).
13. A. L. Stout and D. Axelrod, "Evanescent field excitation of fluorescence by epi-illumination microscopy," *Appl. Opt.* **28**(24), 5237–5242 (1989).
14. B. Richards and E. Wolf, "Electromagnetic diffraction in optical systems. II. Structure of the image field in an aplanatic system," *Proc. Roy. Soc. A* **253**(1274), 358–379 (1959).
15. A. Yoshida and T. Asakura, "Electromagnetic field near the focus of gaussian beams," *Optik* **41**(3), 281–292 (1974).
16. M. Born and E. Wolf, "Electromagnetic theory of propagation, interference, and diffraction of light," in *Principles of Optics*, pp. 370–458, Pergamon Press, Oxford (1975).
17. T. P. Burghardt and D. Axelrod, "Total internal reflection/fluorescence photobleaching recovery study of serum albumin adsorption dynamics," *Biophys. J.* **33**(3), 455–467 (1981).